Numerical prediction of minimum sub-diffraction-limit image generated by silver surface plasmon lenses

Masafumi Fujii[1], Wolfgang Freude[2], and Juerg Leuthold[2]

[1]*Department of Electric, Electronic and System Engineering, University of Toyama,*
3190 Gofuku, Toyama, 930-8555 Japan
[2]*Institute of High-Frequency and Quantum Electronics (IHQ), University of Karlsruhe,*
Engesserstr. 5, 76131 Karlsruhe, Germany

mfujii@eng.u-toyama.ac.jp

Abstract: Sub-diffraction-limit imaging by the surface plasmon polariton (SPP) induced in thin metal film lenses has been analyzed numerically. The SPP images are deteriorated by interference of plasmon fields in layered metal-dielectric structures. To obtain a clear imaging capability, the reflection and the transmission property of evanescent waves in the layered structures has been investigated by the finite-difference time-domain (FDTD) method. For verification, a full 3-dimensional analysis of large-scale layered structures demonstrated sub-wavelength images similar to those obtained in the recently reported experiments. The analysis has been extended further to a lithography of nano-scale images to predict the minimum possible size of the images resolved by the silver thin film lenses.

© 2008 Optical Society of America

OCIS codes: (240.6680) Surface plasmons; (240.6690) Surface waves; (220.3740) Lithography; (160.3918) Metamaterials

References and links

1. J. B. Pendry, "Negative Refraction Makes a Perfect Lens," Phys. Rev. Lett. **85**, 3966–3969 (2000).
2. N. Fang, H. Lee, C. Sun, and X. Zhang, "Sub-diffraction-Limited Optical Imaging with a Silver Superlens," Science **308**, 534–537 (2005).
3. D. O. S. Melville and R. J. Blaikie, "Super-resolution imaging through a planar silver layer," Opt. Express **13**(6), 2127–2134 (2005).
4. T. Taubner, D. Korobkin, Y. Urzhumov, G. Shvets, and R. Hillenbrand, "Near-field microscopy through a SiC superlens," Science **313**(15), 1595 (2006).
5. B. Wood, J. B. Pendry, and D. P. Tsai, "Directed subwavelength imaging using a layered metal-dielectric system," Phys. Rev. B **74**, 115,116 (2006).
6. T. Xu, Y. Zhao, J. Ma, C. Wang, J. Cui, C. Du, and X. Luo, "Sub-diffraction-limited interference photo lithography with metamaterials," Opt. Express **16**(18), 13,579–13,584 (2008).
7. A. D. Rakić, A. B. Djurišić, J. M. Dlazar, and M. L. Majewski, "Optical properties of metallic films for vertical-cavity optoelectronic devices," Appl. Opt. **37**(22), 5271–5283 (1998).
8. A.Taflove and S.C.Hagness, *Computational electrodynamics: the finite-difference time-domain method*, chap. 9, pp. 361–383, 3rd ed. (Artech House, 2005).
9. D. B. Shao and S. C. Chen, "Numerical simulation of surface-plasmon-assisted nanolithography," Opt. Express **13**(18), 6964–6973 (2005).
10. P. A. Belov and Y. Hao, "Subwavelength imaging at optical frequencies using a transmission device formed by a periodic layered metal-dielectric structure operating in the canalization regime," Phys. Rev. B **73**, 113,110 (2006).
11. H. Raether, *Surface plasmons on smooth and rough surfaces and on gratings* (Springer-Verlag, Berlin, 1988).

12. M.Fujii and P.Russer, "A Nonlinear and Dispersive APML ABC for the FD-TD Methods," IEEE Microwave Wirel. Compon. Lett. **12**(11), 444–446 (2002).
13. N. Fang, Z. Liu, T.-J. Yen, and X. Zhang, "Regenerating evanescent waves from a silver superlens," Opt. Express **11**(7), 682–687 (2003).

1. Introduction

Sub-diffraction-limit imaging capability of thin metal films by means of surface plasmon polarization (SPP) that is coupled with evanescent waves has been recently demonstrated theoretically [1] and experimentally [2, 3, 4, 5, 6]. These results have suggested a potential application of the SPP imaging technology to nano-lithography, possibly without using high-energy light sources such as extreme-ultraviolet light. Indeed, the experiments of sub-wavelength imaging has given a significant impact on optics community by substantiating actual negative refractive index materials in optics region.

In spite of the intensive researches conducted so far in this field, it is still unclear how small images the SPP lenses are able to resolve, hence it is necessary to establish a clear guideline of designing the system of layered structures. Since the sub-diffraction-limit imaging deals with nano-scale objects, it is neither straightforward to experimentally obtain sufficiently resolved nano-scale images, nor practical to experimentally examine all the prospective structures and materials. Numerical methods would help predicting the behavior of such layered systems, but it has not been clear yet in regard to with which method and in what conditions the analysis would be reliable.

In order to facilitate convenient numerical analysis methods, the finite-difference time-domain (FDTD) method has been applied to the analysis of the thin metal layered structures. This paper focuses on establishing a numerical technique to simulate the realistic behavior of SPP on actual metal thin films, and clarify reflection and transmission of evanescent fields in thin metal and dielectric layered structures, in particular, the field distribution inside metal layers. In addition, solutions of large scale layered systems demonstrate reproducing the previously reported experimental results.

To model the dielectric properties of metals in optics region, we have employed the precise Lorentz-Drude dispersion functions of various metals [7], which are based on experimental data of complex dielectric permittivity up to 5 to 6 eV. The Lorentz-Drude models have been implemented into the FDTD method by the auxiliary differential equation technique [8]. Although a similar analysis has been reported so far [9, 10], in this paper the direct lensing effect of silver (Ag) films is analyzed by employing the precise Lorentz-Drude models of metals. Moreover, not only the field on the cross section of layered structures, but also the true two-dimensional images have been demonstrated. Based on these analyses as verification, the method is applied to the analysis of nano-scale lithography patterns to predict the theoretical limit of the imaging resolution; it suggests the applicability of the method to the actual lithography technology.

2. Sub-diffraction-limit imaging of gratings and slits by a silver thin film

Previous experimental research [2, 3] has successfully demonstrated fine-resolution imaging of gratings by using silver thin films below or at the comparable level of the diffraction limit. In this section the similar grating structures [2] are analyzed by the FDTD method, and the distribution of the light field inside the layered structure is observed. In our calculation, precise Lorentz-Drude models of dielectric permittivities [7], which have been obtained by fitting experimental data up to high enough photon energy, are used for silver and chromium. The frequency dependent permittivity is shown for silver in Fig. 1; in this model the plasma energy locates at 3.828 eV (plasma frequency $\omega_p = 925.5$ THz).
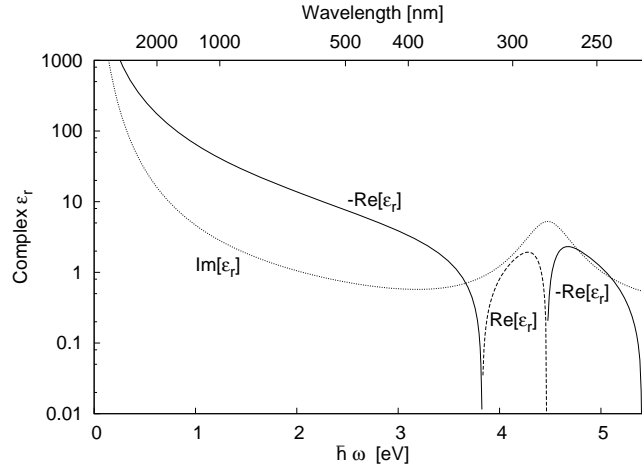
Fig. 1. The Lorentz-Drude model of the complex relative permittivity of silver.

To verify the FDTD analysis of SPP, the dispersion relation of SPP on a silver film of thickness 35 nm has been analyzed with different grid sizes Δ by adopting the complex permittivity model of Fig. 1. The silver layer is sandwiched by dielectrics of relative permittivity $\varepsilon_r = 1.9$, which has been chosen because silver has the real part of its complex permittivity -1.9 at wavelength 365 nm. Although, in the following sections, dielectrics of slightly different permittivities will be used for designing the layered structures, the present results of the SPP dispersion would in general give guidelines regarding the accuracy and necessary analysis conditions.

The FDTD results have been compared with analytical solutions [11] in Fig. 2. For the grid size of $\Delta = 5$ nm the results of the frequency contain approximately 5% errors at large wave numbers. However, the analysis results still hold a reasonable qualitative tendency. For $\Delta = 2.5$ nm and 1.25 nm, the results agree well, and convergence has been obtained.

In the following analysis of imaging for a grating pattern, $\Delta = 2.5$ nm is chosen. The sizes of the grating analyzed here are similar to those in [2]; and the layer thicknesses are identical as shown in Fig. 3. However, one parameter is unknown, which is the dielectric constant of the top photo-resist layer; after preliminary calculations, a typical value of $\varepsilon_r = 2.1$ has been tentatively chosen; the other permittivities are $\varepsilon_r = 2.4$ for polymethylmethacrylate (PMMA), and 2.1 for silica grass substrate. Then a UV light at wavelength 365 nm is illuminated from underneath the substrate, with linear polarization directed perpendicular to the direction of the grating slit. In the numerical analysis, the whole layered structure is surrounded by a nonlinear perfectly matched absorbing layer (PML) boundary condition [12]. For clearly detecting the resulting images, the energy dissipated in the photo-resist layer

$$W = \int_0^T \sigma |E|^2 dt , \qquad (1)$$

with assuming $\sigma = 1$, is calculated; the value $\sigma = 1$ is tentatively chosen because it allows direct observation of the field distribution. In Fig. 4, the distribution of W at height 180 nm for the maximum time duration $T = 20$ fs is plotted on top, and the same quantity on the cross section of the layered structure is plotted underneath.

For the periodic structure, the image is nicely resolved, as demonstrated typically in experiments. The full width at half maximum (FWHM) of the image profile is 80 nm while the width of the slit is 60 nm. It is interesting to note that in the bottom figure, a focusing effect of evanes-
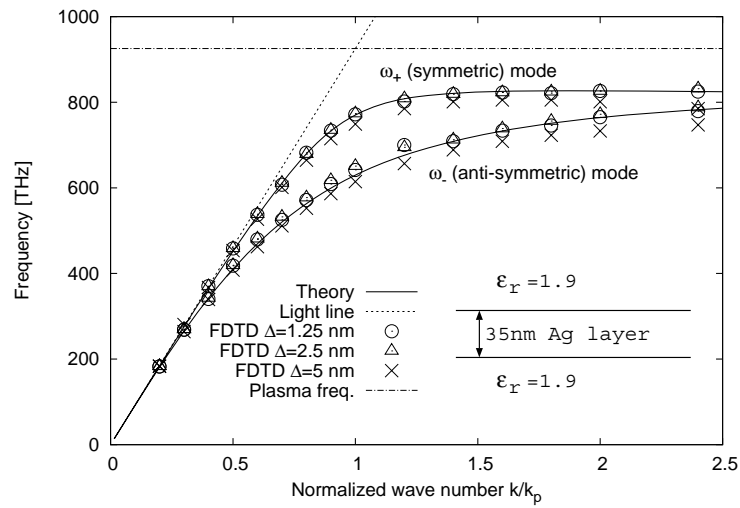
Fig. 2. Dispersion relation of SPP on Ag film. The horizontal dash-dotted line indicates the plasma frequency at 925.5 THz. The inset shows the cross section of the analyzed layered structure.
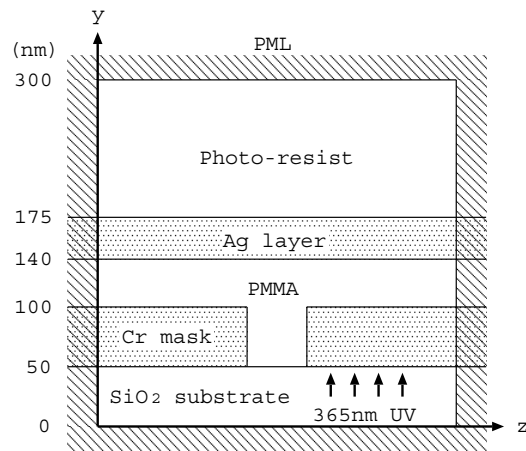

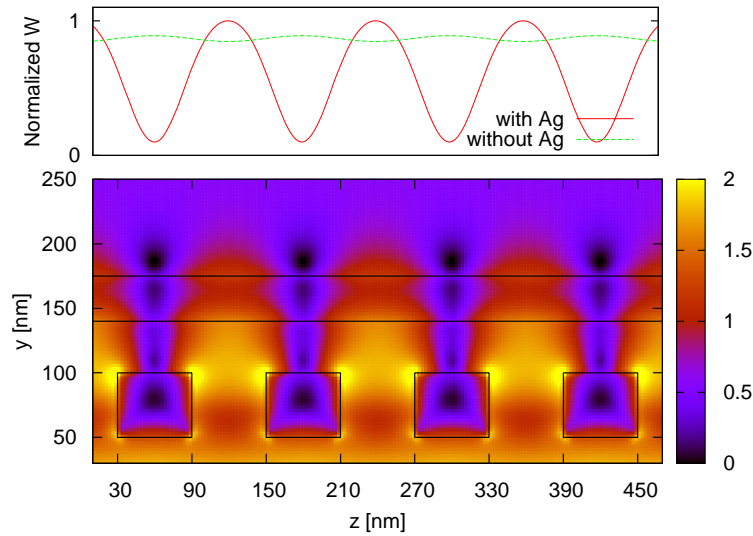Fig. 3. The layer structure of the experiment by Fang. et.al. [2] considered also in this paper.

Fig. 4. Imaging of a grating (60 nm wide slit and 60 nm wide Cr mask). Top: a linear scale profile of the grating image obtained by integrating the energy dissipation W in the photo-resist layer observed at height 180 nm. The image profile for the case of no silver layer is plotted for comparison. Bottom: the distribution of W on the cross section in a logarithmic magnitude color scale. The black solid lines indicate the boundaries of the Ag film (140 nm to 175 nm in height) and Cr mask of the grating (50 nm to 100 nm in height).

cent light is observed in the silver layer, and also above the silver layer, the field appears to form a focal point for each slit.

However, for a non-periodic structure, which is obtained by eliminating all the slits from the chromium (Cr) mask except one, an imaging of a single slit is obtained as in Fig. 5. Unlike for the grating of Fig. 4, the image of the slit broadens to FWHM 161 nm, and interestingly the field in the silver layer appears to split into two high-intensity regions. This may influence the image resolution by the silver layer. For comparison, the image profile is shown in Fig. 5 (top) also for the case where the silver layer is replaced by PMMA; in this case FWHM is even smaller. However, the energy dissipation W in photo-resist is larger when the silver layer exists. The reason will be considered in the next section. The other case is with 25 nm thick silver layer; on the photo-resist layer at height 180 nm, the detected energy dissipation W is slightly larger than that with the 35 nm thick silver. Thus the design of the layered structure is not straightforward, and needs more detailed consideration.

3. Image splitting phenomena of thin metal lens systems

In order to clarify the effects of the dielectric permittivity and the thickness of the layers to the imaging property, a simple Drude metal of thickness 50 nm is tested, i.e. the relative permittivity of the metal is given by a real function

$$\varepsilon_r = 1 - \frac{\omega_p^2}{\omega_o^2} \,, \tag{2}$$

with the plasma frequency $\omega_p = 925.5$ THz that is as same as silver, and the operating frequency ω_o was chosen to be 585.3 THz to give $\varepsilon_r = -1.5$. Two dielectric layer configurations are
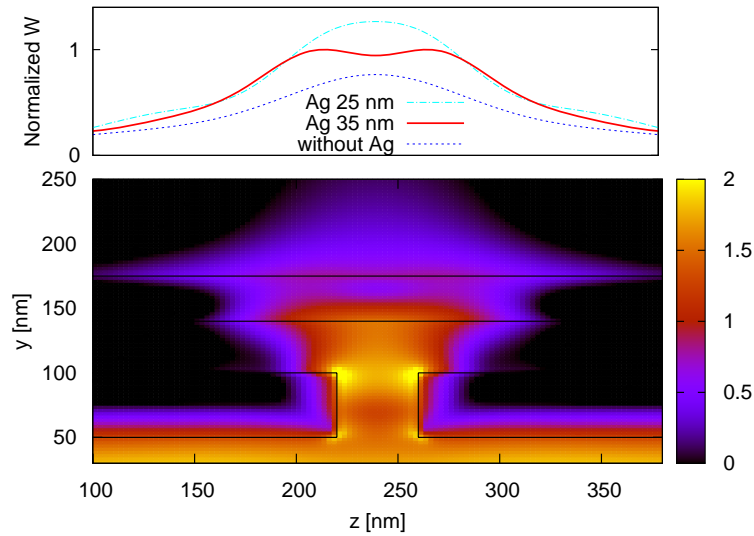
Fig. 5. Imaging of a 40 nm wide single slit. The plots has been prepared similarly as in Fig. 4. Top: comparison of normalized W for the three cases of 35 nm thick Ag layer (FWHM 161 nm), 25 nm thick Ag layer (FWHM 111 nm), and without Ag layer (FWHM 135 nm). Bottom: the distribution of W in a logarithmic magnitude color scale for 35 nm thick Ag layer system.

considered: the one has $\varepsilon_r = 2$ for the top photo-resist, -1.5 for the Drude metal, and 1 for the bottom layer below the Drude metal; the other has the opposite order in ε_r, i.e, 1 for photo-resist, -1.5 for Drude metal, and 2 for the layer below the Drude metal. The metal layer locates from height 50 nm to 100 nm as shown in Figs. 6 and 7. Interestingly, these two dielectric systems give significantly different field distributions in the layered structure, shown in Fig. 6 where the field appears to split, and in Fig. 7 where the field appears to focus.

After analyses of various layered structures, it has been found that when a light enters from a low dielectric constant region to a high dielectric constant region, in terms of the absolute value for the negative permittivity, the field appears to split. In contrast, when a light enters from a high dielectric constant region to a low dielectric constant region, it appears to focus. However, interestingly the FWHM is smaller for the former case. This is also shown in Fig. 8. When the metal thickness becomes smaller, the image becomes sharper. In this figure, the smallest FWHM of 68 nm and highest contrast is obtained for the metal thickness of 30 nm and $\varepsilon_r = 2$ for the top, -1.5 for the metal, and 1 for the bottom layer.

The effect of field splitting is no longer seen in Fig. 8 when the metal thickness reduces to 30 nm. However, the field splits inside the layered structure, and the split fields superimpose above the metal layer to form a single peak.

The field splitting and focusing phenomena may be explained partly by the differences in the reflection and transmission coefficients calculated by the Fresnel formula. For a p-polarized (or transverse magnetic, TM) light, the Fresnel reflection and the transmission coefficients are calculated using the standard formula also given in [13], with more clarification in definitions for a light entering from layer 'm' to 'n', having a complex relative permittivity $\varepsilon_{r,m}$ and $\varepsilon_{r,n}$,
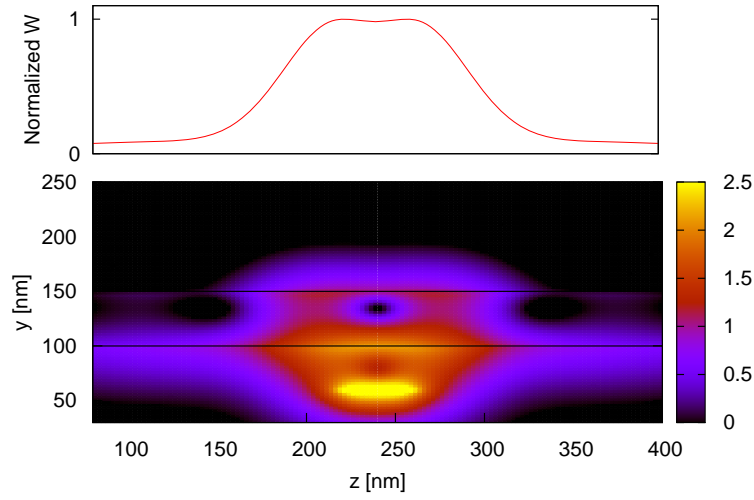
Fig. 6. Splitting field in the 3-layered structure of $\varepsilon_r = 2$ for the top, -1.5 for the metal, and 1 for the bottom layers. Top figure: normalized W detected at height 155 nm. Bottom figure: the distribution of W plotted in a logarithmic magnitude color scale. An excitation source of 40 nm in width locates at height 60 nm. The black solid lines indicate the boundaries of the metal layer.
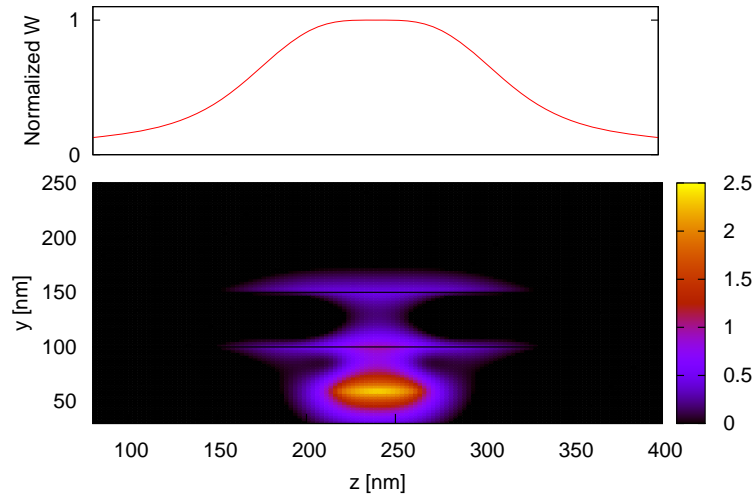

Fig. 7. Focusing field in the layered structure of $\varepsilon_r = 1$ for top, -1.5 for metal, and 2 for bottom. Top figure: normalized W detected at height 155 nm. Bottom figure: the distribution of W in logarithmic magnitude color scale. Same excitation source as in Fig. 6.
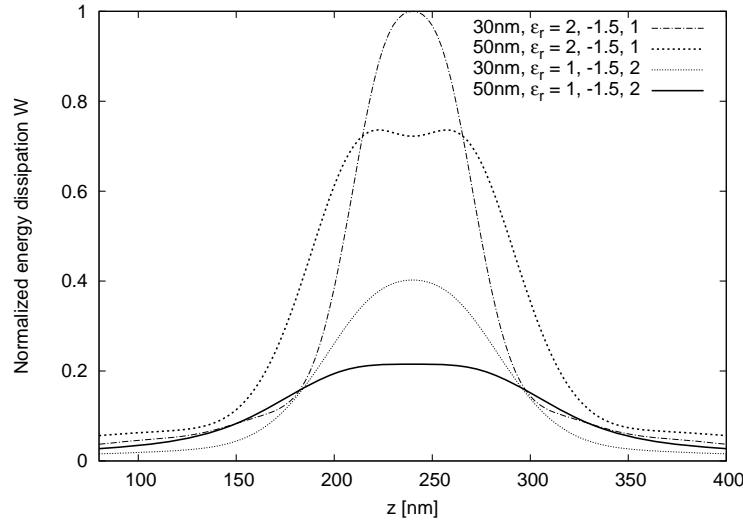
Fig. 8. Comparison of the single slit image profiles by energy dissipation W for four types of layered systems. The thickness of the Drude metal is 50 or 30 nm, and the layered structures are $\varepsilon_r = 1$ for the top, -1.5 for the metal and 2 for the bottom layers, or ε_r opposite in order, i.e. 2, -1.5, and 1, respectively. The plots are normalized by the largest W for 30 nm thick $\varepsilon_r = 2$, -1.5, 1. The profiles were detected at 5 nm above the metal surface.

respectively,

$$r_{mn} = -\frac{\frac{k_{z,m}}{\varepsilon_{r,m}} - \frac{k_{z,n}}{\varepsilon_{r,n}}}{\frac{k_{z,m}}{\varepsilon_{r,m}} + \frac{k_{z,n}}{\varepsilon_{r,n}}} , \tag{3}$$

$$t_{mn} = 1 + r_{mn} \tag{4}$$

where $k_{z,m}$ is the wavenumber in layer 'm' in the direction (z) normal to the layer, as given later for our particular case. The overall reflection and transmission coefficients for a 3-layered structure of dielectric-metal-dielectric configuration are given respectively by

$$R = r_{12} - \frac{t_{12}^2 r_{23} \exp(2ik_{z,2}d)}{1 + r_{12}r_{23}\exp(2ik_{z,2}d)} , \tag{5}$$

$$T = \frac{t_{12}t_{23}\exp(ik_{z,2}d)}{1 + r_{12}r_{23}\exp(2ik_{z,2}d)} , \tag{6}$$

with the wavenumber $k_{z,m}$ for layer 'm', and k_x, which is the wavenumber tangential to the layers as identical to the notation in [13], i.e.

$$k_{z,m} = \begin{cases} \sqrt{\dfrac{\varepsilon_{r,m}\mu_{r,m}\omega^2}{c^2} - k_x^2} , & \text{for } m = 1,3 \\[2mm] i\sqrt{k_x^2 - \dfrac{\varepsilon_{r,m}\mu_{r,m}\omega^2}{c^2}} , & \text{for } m = 2 \end{cases} . \tag{7}$$

The coefficients are plotted in Figs. 9 and 10. It is interesting to note that in Fig. 10 where a light enters from high ε_r to low ε_r, total reflection occurs at 45 degree incident angle. When total reflection occurs, the field that contributes to the imaging through a metal layer is restricted

relatively in a small region. However, for the opposite configuration of Fig. 9, all the fields enter into the layered system at any angle, and contribute to the imaging with an angle-dependent transmission property.

We note here the interpretation of these results from a view point of evanescent and propagating waves. In FDTD analysis, fields are obtained in real numbers, and both evanescent and propagating waves are taken into consideration in Figs. 6 and 7. The Fresnel coefficients of Figs. 9 and 10 have been obtained by not restricting to either propagating or evanescent wave, as discussed in [1], in other words, our assumption is that permittivities of dielectrics are positive and that of metal is negative. Hence the results of the Fresnel coefficients are effective for both propagating and evanescent waves. It is therefore concluded that the field evolution in Figs. 6 and 7 reflects the results of Figs. 9 and 10; i.e. in Fig. 7 the field energy accumulates in the vicinity of the light source, while in Fig. 6 the field spreads over a wide region, and then contributes to the image above the metal layer. These differences in the reflection and transmission properties may explain the behavior of the field in the layered system.
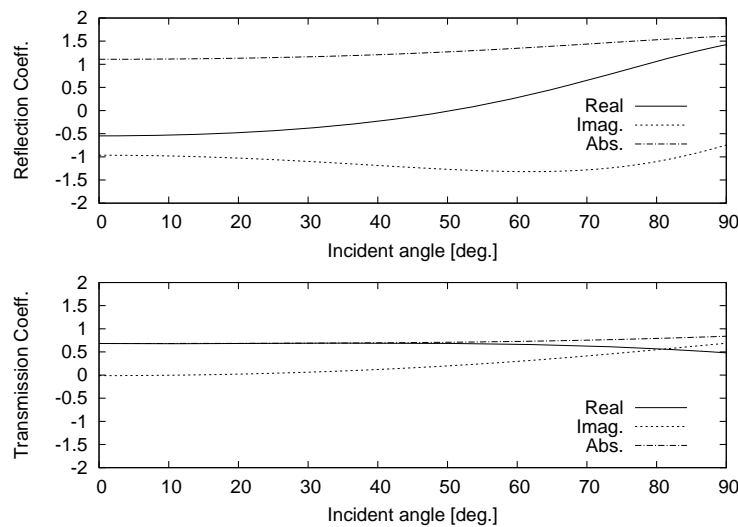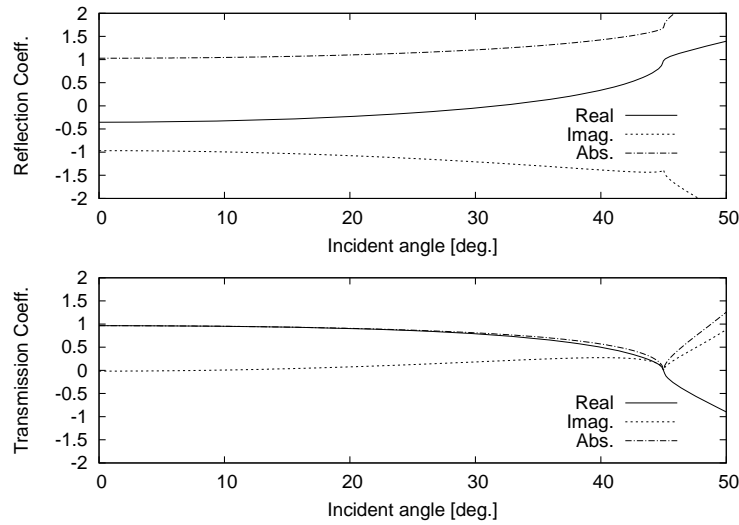

Fig. 9. Overall Fresnel reflection and transmission coefficients R and T, for the layered structures of $\varepsilon_r = 2$ for top,-1.5 for the metal, and 1 for bottom. Real, imaginary and absolute values are plotted.

4. Full 3D analysis of sub-diffraction-limit imaging by a silver thin film

In this section, a full 3D analysis of the sub-diffraction limit imaging is performed for a large structure of which mask layer is carved with an alphabetical letter [2]. The dielectric permittivity for the top photo-resist layer is chosen to be 2.1 or 1.5. Imaging of a letter 'T' was analyzed, although others such as 'O' and 'P' were tested. All of them had shown a similar imaging property. The light source in the numerical analysis is typically coherent, while for experiment it is a 365 nm line from a mercury lamp; in order to realize a similar effect of incoherent and arbitrary polarized source, a circularly polarized source is employed. This is realized by using two orthogonally polarized sources with 90 degree phase difference.

The pattern of letter 'T' is an aperture on the chromium mask with the slit width of 40 nm. The size of the analysis region is 3 μm$\times$ 3 μm, and that of the letter is 2.6 μm$\times$ 2.6 μm (see Fig. 11). The calculation was performed for the time duration of 10 fs, and convergence

Fig. 10. Overall Fresnel reflection and transmission coefficients R and T, for the layered structures of $\varepsilon_r = 1$ for top, -1.5 for the metal, and 2 for bottom. Real, imaginary and absolute values are plotted. Total reflection is observed at the incident angle of 45 degrees.

is obtained. The snapshots of the electric field detected on the photo-resist layer are shown in Fig. 12. It is interesting to note that the fields show diffraction-like multiple images of the letter, possibly due to the multiple reflection of the fields caused by the layer boundaries.
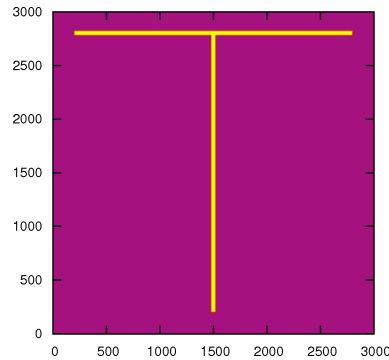
Fig. 11. Mask pattern of letter 'T'. The purple part is chromium, and the yellow is the slit filled with PMMA ($\varepsilon_r = 2.4$.)

The field decays strongly with the distance from the silver layer. In the FDTD analysis, the field components have different heights whether it is tangential (E_x and E_z) or perpendicular (E_y) to the silver surface. It is noted in Fig. 12 that E_y field exhibits relatively stronger field than the others. E_y is obtained by averaging the fields at nodes half a cell upper and half a cell lower. Therefore, the field normal to the metal surface may result in a stronger value than the tangential fields. In order to compensate such effects, a field amplitudes of $|E|^2 = E_x^2 + E_y^2 + E_z^2$ and $|E|^2 = E_x^2 + E_y^2/4 + E_z^2$ are detected and integrated in time. The resulting images for both cases are compared in Fig. 13 for the case of using a silver layer, and in Fig. 14 for not using a silver layer. The resulting images are found to exhibit similar properties as those obtained

experimentally in [2]. However, FWHMs of the straight part of the line are approximately 200 nm for both with and without a silver layer when integrating each field equally as $|E|^2 = E_x^2 + E_y^2 + E_z^2$. Contrary, for integrating $|E|^2 = E_x^2 + E_y^2/4 + E_z^2$, FWHMs are approximately 60 nm with a silver layer and 120 nm without a silver layer, which may seem too narrow compared to the experimental results. Considering that the width of the slot is 40 nm, sharper images may be obtained. This is the point that needs further consideration.

It is noted in general that when SPP is analyzed by the FDTD method, an artificial enhancement of fields is observed occasionally, in particular when the group velocity of SPP is close to the velocity of the plane wave in free space. The origin of such numerical error has been already characterized by the authors. Although the discussion of this error goes beyond the scope of this paper, it is often due to the coupling of the SPP field with a plane wave, and successive interaction with the perfectly matched layer (PML) absorbing boundary condition, which is known to be inefficient for waves propagating laterally to the boundary, thus it is necessary to carefully model the structure. In the present analyses, the operating frequency of the imaging is in the region where the group velocity of SPP is much lower than that of the plane wave. Therefore the numerical errors of the above mentioned origin is considered to be negligible.
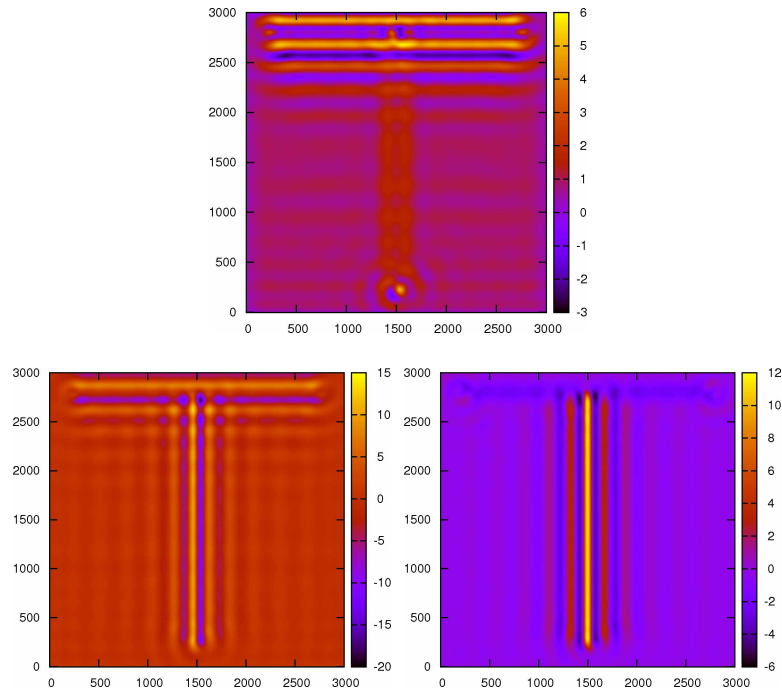

Fig. 12. Electric fields of letter 'T' obtained with silver thin film. Top:E_x, bottom left;E_y and bottom right:E_z.

5. Sub-diffraction-limit imaging of nano-scale lithography patterns

Based on the validation in the previous section, the analysis method has been applied to some nano-scale lithography patters. In experiment it would be difficult to optimize the fabrication process and materials. The numerical analysis would predict for what types of patterns and to which extent the layered metal-dielectric structure resolves fine images.

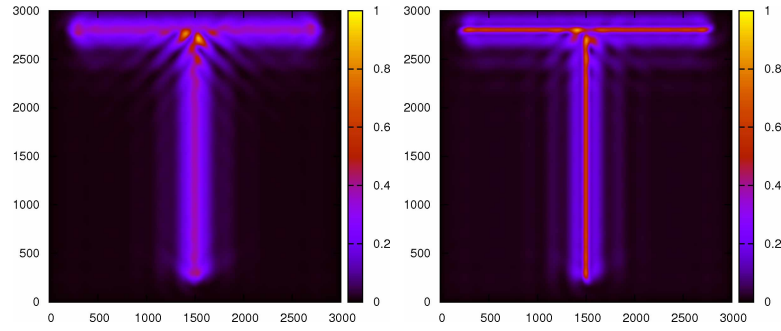For the letter 'T' shape in the previous section, the field coming out of the slit maintains the

Fig. 13. Image of letter 'T' obtained by calculating W in the photo-resist layer with the silver layer. Left figure is obtained by integrating $|E|^2 = E_x^2 + E_y^2 + E_z^2$, and right figure obtained by modified field $|E|^2 = E_x^2 + E_y^2/4 + E_z^2$.
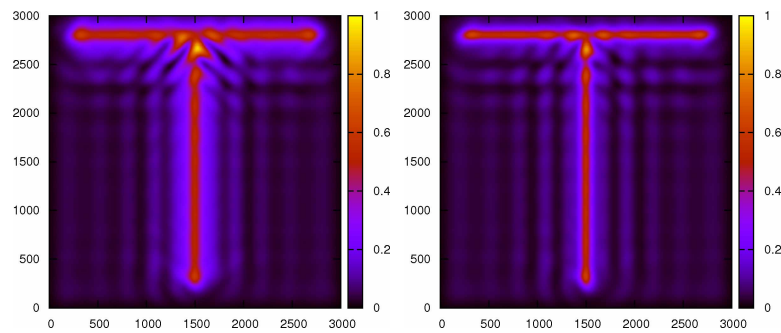

Fig. 14. Image of letter 'T' obtained without the silver layer. Left and right figures obtained similarly as in Fig. 13.

direction of polarization uniformly at sufficiently long and straight part of the slit. However, at the point of crossing or at the edge of a slit, the polarization of the field is disturbed, and in consequence, it results in a deformed image. Therefore, it is not straightforward to regenerate an image for a lithography pattern that is small in size.

The patterns tested in this section are round holes, a ring, and a plus shaped slit, all of which are much smaller in size than that in the previous section. The layered structure is identical as that of the literature [2] and the previous sections. The mask pattern and the resulting images are shown in Figs. 15, 16,17 and 18. The sizes of each pattern are described in the corresponding figure captions. In the analysis a circularly polarized source is used, which allowed more clearly resolved images of round shapes, rather than using a linearly polarized source. The images are detected at a plane 5nm above the metal surface, for which the best resolution is obtained. when the plane of detection moves to more than 10 nm above the metal, the image broadens gradually.

For a simple round hole of 40 nm diameter (Fig. 15), the effect of the silver layer is obvious, the FWHM of the images are 119 nm with a silver layer, and 261 nm without a silver layer. When two holes locate closely, the fields from each holes interfere, and in this case the distance between the holes is 167 nm, and the images of the holes are well resolved, and the FWHM for one of the hole images is 126 nm. However, without a silver layer, only a single large image is observed. The example of a ring slot demonstrates the minimum FWHM of 84 nm with a silver layer, and 126 nm without a silver layer. The last example of a plus shaped slit of Fig.18 shows a peculiar result; due to the circularly polarized source, the image also rotates slightly.

For complicated slot patterns like the plus shape, the resulting images were mostly deteriorated. This can be due to the interference of the SPP fields on the silver film. In this particular case, the interference worked in such a way that the SPP wave from each section of the slot enhanced each other.

These results show the advantage of employing a silver thin layer as a lens; images of sharper contrast and clearer resolution are obtained for patterns having features of 100 nm in size or less. Our additional analyses showed that most of the patterns resulted in distorted images. However, by somehow controlling the phase of the SPP waves, there may be possibility of producing better imaging capability.
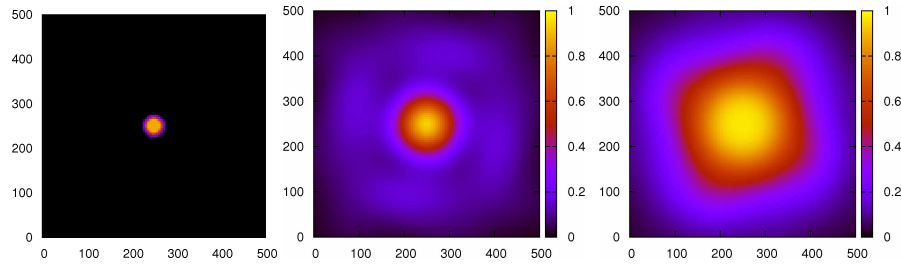

Fig. 15. Mask pattern (left) of a 40 nm diameter hole, and the images obtained with (center) and without (right) a silver thin layer.
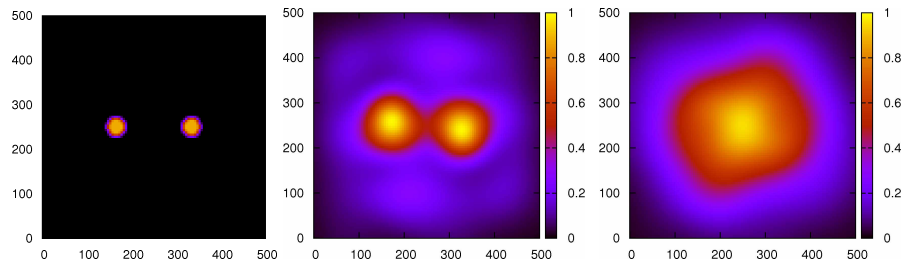

Fig. 16. Mask pattern (left) of two 40 nm diameter holes, and the images obtained with (center) and without (right) a silver thin layer.
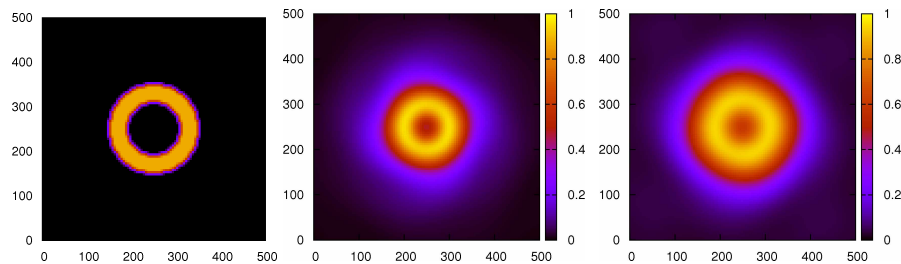

Fig. 17. Mask pattern (left) of a ring of 60 nm inner radius and 100 nm outer radius, and the images obtained with (center) and without (right) a silver thin layer.

6.   Conclusion

By applying the FDTD method together with the precise complex permittivity model of metals, the sub-diffraction-limit imaging by thin silver films has been demonstrated. The origin of the
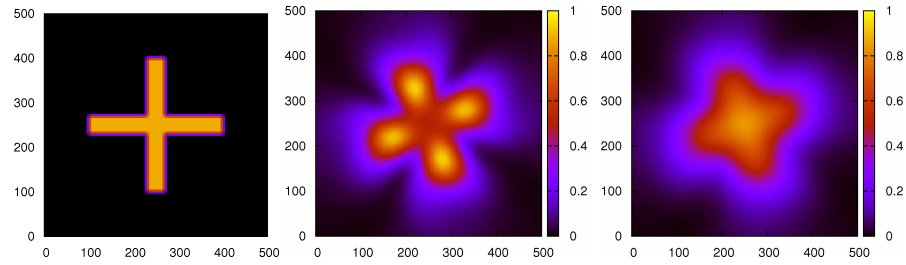
Fig. 18. Mask pattern (left) of 40 nm wide plus shaped slits, and the images obtained with (center) and without (right) a silver thin layer.

deterioration of images such as field splitting has been considered. Guidelines for numerical analysis using the FDTD method and those to improve the image quality by choosing proper dielectric constants have been suggested. The resulting image obtained from the 3-dimensional calculation reproduces well the properties observed in the previously reported experimental results. The analysis of nano-scale patterns suggested also a possibility of resolving images as small as 100 nm or less.

Acknowledgments